6.1 Introduction

In the modern era of information technology (IT), to accomplish the requirement of robust, energy-efficient and high-capacitive storage devices like cloud storage, spintronics technology has arrived with a relatively feasible solution [213]. Meanwhile, racetrack memory devices emerged with radically enhanced bit densities employing the domain walls as the transporters of information certainly reducing the consumption of energy and enhancing the access time. Another eminently relevant and auspicious discovery in the field of topological matter is the magnetic Skyrmion. Eventually, Skyrmions represent topologically protected field configurations with particle-like characteristics providing enormous stability even at the nanoscale. Such vortex-like whirling nano-object in non-centrosymmetric non-trivial metallic helimagnet displaying topologically invariant spin texture represents it as a potential carrier of information in future high-density data storage devices, ultrafast spintronics and microwave devices. Irrespective of such amusing properties, the utilization of Skyrmions has not been accomplished yet as spintronic devices. There are several shortcomings related to the current-driven motion of such magnetic particles and the restricted region of Skyrmions phase-space (*H*-*T*).

In such a system, an extremely small current is required to modify the spin configurations by the virtue of the small domain size. As a result, such materials hold great promise for information technology. Subsequently, the challenge is to discover the specific operating region of Skyrmion in the magnetic field (*H*) - temperature (*T*) phase space and somehow expand the functional range. The complicated struggle amidst the exchange interaction, DM spin-orbit interaction and anisotropic crystallinity in a non-centrosymmetric helimagnetic compound develops the field temperature (*H*-*T*) phase diagram. This exclusive property enlarges the utilization space of such materials as high-potential information devices, drastic spintronics and dynamic microwave devices.

$Co_3Sn_2S_2$ is a shandite-type compound possessed with Kagome sub-lattices that initiated an unconventional magnetic phase below its ferromagnetic transition temperature. This phase induces a spin state which is non-trivial at low-field *H-T* phase space [65]. Earlier literature assured the possibility to tune the stability of the Skyrmion phase in a Skyrmion lattice to a broader and higher-temperature region by the implementation of uniaxial strain [68]–[71], chemical substitution [63], [72]–[75], physical or chemical pressure [59]. Also, a certain magnetic anomaly was presented as a signature of the non-colinear Skyrmionic phenomenon by *H. C. Wu et al* with the application of a very low magnetic field under physical or chemical pressure. They further depicted an *H-T* phase diagram recognizing the Skyrmion phase in $Co_3Sn_2S_2$ originated by magnetic susceptibility measurement [76]. Such stimulating discoveries introduce the magnetic WSM $Co_3Sn_2S_2$ as a promising applicant in spin-frustrated systems exploring the isentropic and isothermal magnetic moment below the ordering temperature.

In the present article, we have demonstrated the consequences of the chemical pressure effect on the isothermal and isentropic magnetization, M (H, T), and AC susceptibility, χ_{ac} (H, T, f) in $Co_3Sn_2S_2$ Kagome ferromagnets systematically and the existence of a low-field anomalous but equilibrium magnetic phase just below T_C. The anomalous phase displays slow spin dynamics signifying that the inconsistent phase has a Skyrmion-like nontrivial spin texture. Such a topologically invariant chiral spin helical state arises below a T_C with a certain periodicity initiated by a competition between the FM/AFM interchange and antisymmetric Dzyaloshinskii-Moriya interactions. Eventually, our purpose is to create chemical pressure by replacing S with a relatively heavier molecule like Se to examine the modification of the magnetic properties in the microstructural domains and to achieve a wider temperature range of the Skyrimionic phase. However, it has been observed, that the present system provides a significant development in the

Skyrmion phase range (*ΔH-ΔT*) simply introducing chemical tension by creating interstitial disorders. Other than that, we have succeeded to achieve the mysterious magnetic phase with the application of an exceptionally small magnetic field concerning the Se doping concentration.

6.2 Experimental

$Co_3Sn_2S_{2(1-x)}Se_{2x}$ (x = 0, 0.25, 0.5) crystals were synthesized by the modified Bridgeman technique as described earlier in section 2.2.1. In this procedure metal based high-purity Co (99.99%) powder, Sn (99.99%), S (99.97%) and Se (99.99%) granules were mixed in appropriate stoichiometric ratio followed by vacuum sealing (under ~10^{-5} mBar pressure) in quartz ampules of 13.8 cm length, 2 cm diameter, 0.2 cm thickness and with a conical tip of 1.8 cm. The sealed ampules were placed into a muffle furnace, heated to 700 ºC and stabilized at that temperature for 24 hours followed by slow heating to 1050 ºC for melting. After staying at 1050 ºC for 24 hours they were slowly cooled down to 800 ºC at the rate of 4 ºC per hour intended for better growth of crystals. Further, they were annealed at 800 ºC temperature for 48 hours and air quenched to room temperature. In this manuscript, as prepared $Co_3Sn_2S_{2(1-x)}Se_{2x}$ (x = 0, 0.25, 0.5) crystals are symbolized as CSSS, CSSS25 and CSSS50 respectively. The grown crystals were initially ground to perform powder X-ray diffraction (XRD) measurement to identify the structure and phases with CuK_α radiation using a Rigaku (Mini Flex II DESKTOP) powder diffractometer. In addition, we used Foolproof and VESTA software to analyze and accumulate the structural information related to our system. Further, a magnetic property measurement system (MPMS 3 SQUID magnetometer) was used to distinguish the magnetic properties of the prepared systems. To be more specific, we recorded the temperature-dependent magnetization (*M-T*) data under the application of varying magnetic field (*H*) in two ways as follows: first, the sample was cooled down to a minimum temperature 2.2 K from 300

K under zero field and then recorded data during heating under a certain magnetic field to obtain zero field-cooling (ZFC) magnetization at a heating rate of 5 K/minute. Second, the sample was cooled under a certain field, and recorded the data during heating cycle to obtain field-cooling (FC) magnetization. Then, field-dependent magnetization (*M-H*) data were recorded at a rate of 60 Oe/second from -5 T to 5 T field (total five quadrants) by stabilizing at different temperatures. Further, AC susceptibility was measured with temperature (χ_{ac}-*T*) at different frequencies and applied fields during the heating cycle at a rate of 1.5 K/minute using the ZFC condition. Also, magnetic field-dependent AC susceptibility (χ_{ac}-*H*) was recorded at different temperatures with a sweep rate of 8 Oe/second, where AC frequency (f_{ac}) was fixed at 10 Hz and a very small AC field (H_{ac} = ± 3 Oe) was applied.

6.3 Results and Discussion

6.3.1 Structural Characterization

The powder XRD patterns corresponding to $Co_3Sn_2S_{2(1-x)}Se_{2x}$ (x = 0, 0.25, 0.5) crystals, refined with the Rietveld method are shown in Figure 6.1 (a-c), respectively. The corresponding lattice parameters and Rietveld fitting parameters are listed in Table 6.1. Here, $Co_3Sn_2S_2$ contains Co-Sn metallic layers which are stacked periodically along the *c* axis in the rhombohedral shandite structure ($a = b \neq c$, $\alpha = \beta = 90^\circ \neq \gamma = 120^\circ$) with $R\bar{3}m$ *(166)* space group [76], [214], [215]. Each layer consists of a two-dimensional (2-D) network of corner-sharing triangular frameworks organized as a 2-D Kagome sub-lattice [20], [216]–[218] as shown in Figure 6.1 (d). The corners of the triangle are occupied by geometrically frustrated Co atoms with Sn at the center and each Co atom is shared by two adjacent units. Thus, three Co atoms along with one Sn atom constitute one Kagome unit. The Kagome layer is disjointed by Sn1 (interlayered Sn) - Sn2 (Sn in the Kagome layers)

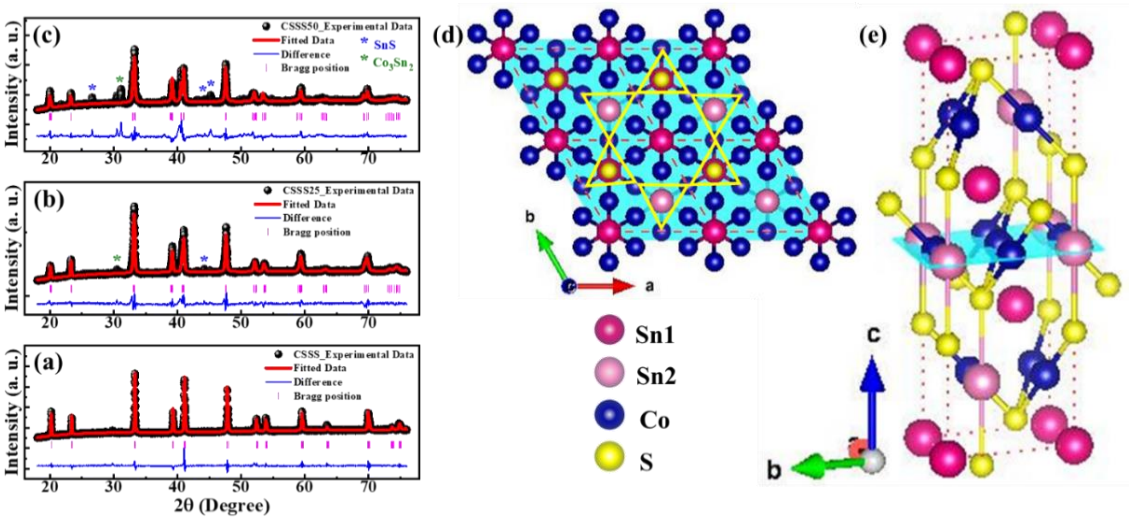

Figure 6.1: Powder XRD patterns corresponding to (a) CSSS, (b) CSSS25 and (c) CSSS50 along with the Rietveld refinement fitted data are shown. (d) Shows the Kagome lattice plane indicating the corner sharing Co atoms with Sn at the center. (e) One unit cell of CSSS lattice presenting all atoms and bonds associated with it.

Table 6.1 The powder XRD refinement parameters correspond to CSSS, CSSS25 and CSSS50 rhombohedral structure and R$\bar{3}$m space group.

Refinement parameters	CSSS	CSSS25	CSSS50
a = b (Å)	5.372313	5.387924	5.38589
c (Å)	13.185669	13.289931	13.342827
V (Å^3)	380.561442	385.803043	387.046205
Z	0.28915	0.28798	0.29464
χ^2	5.11	6.49	15.7
R_{Bragg}	1.53	1.59	1.57
R_{Factor}	2.14, 3.45	2.77, 4.04	3.98, 6.23
R_p	34.7	39.9	61.1
R_{wp}	20.3	24.3	39.1

and the S atoms are situated above and below the Co base trigonal anti-prismatic configurations in the Kagome layer [219]–[222]. Such a Kagome lattice structure was predicted to host mysterious quantum magnetic states like Dirac electronic states leading

to the topological and Chern insulating phases [223]–[226]. The Wyckoff positions corresponding to each atom are portrayed as Sn1 ~ (0, 0, 0), Sn2 ~ (0, 0, 0.5), Co ~ (0.5, 0, 0.5), S/Se ~ (0, 0, z) for all 3 crystals and exhibited in a single unit cell of CSSS in Figure 6.1 (e). However, such a 2-D array of neighboring unit cells (Figure 6.1 (d)) and three-dimensional (3-D) structure of CSSS (Figure 6.1 (e)) were constructed by compiling VESTA software using the CIF output file of Rietveld refinement via Foolproof software. Nevertheless, the CSSS25 and CSSS50 crystals reveal the same shandite-type rhombohedral ($R\bar{3}m$ space group) structure as the main phase with minor impurities associated with SnS and Co_3Sn_2 as has also been observed in some other reports for $Co_3Sn_2S_2$ [76], which are marked in Figure 6.1 (b) and Figure 6.1 (c). Also, the volume of the unit cell increases certainly with growing Se concentration in the S site. Such volume expansion may happen due to the bigger size of the Se atoms with respect to the S atoms, which creates an interstitial defect in the crystal structure. Such interstitial disorders introduce certain stress on the crystal chemically. This chemical pressure may affect the present Kagome structure by reorienting the magnetic ions and upsurging the stability of the Skyrmion phase, which is described in the next section.

6.3.2 Magnetic Characterization Introducing the Skyrmion Phase

In order to investigate the proposed Skyrmion phase in the formulated magnetic Kagome-type WSM systems, we examined the magnetic moment and susceptibility of the systems with varying temperatures and fields in detail. Figure 6.2 (a-i) exhibits the temperature and magnetic field dependency over the magnetic moment for all three systems. Here, the temperature-dependent magnetic moments driven at ZFC and FC conditions with applying magnetic fields ranging from 50 Oe to 500 Oe for pure CSSS system are displayed in Figure 6.2 (a). With the application of H = 500 Oe the ZFC M-T

curve demonstrates a sharp magnetic transition adjacent to 176 K. The discontinuity occurred to the 1st order derivative of magnetic moment with respect to temperature *(dM/dT*) as shown in the inset of Figure 6.2 (b) and the minima of this curve is defined as magnetic transition temperature, T_C (176.51 K) which is consistent with the previous literature [20], [227], [228]. At lower *H*, the magnetic moment decreases monotonously and we can observe a hysteresis between ZFC and FC *M-T* curves with a large bifurcation (shown for H = 200 Oe in Figure 6.2 (a)) below T_C. The difference between ZFC and FC *M-T* curves gradually reduces with the enhancement of the applied field confirming that a strong magnetic anisotropy in the system is the reason behind the bifurcation that occurred below T_C. Though the observed transition is 2nd order paramagnetic (PM) to ferromagnetic phase transition, the existence of a local minimum adjacent to 142 K in the ZFC magnetization curves at H = 500 Oe, 200 Oe and 50 Oe is quite different from the conventional transition indicating the presence of a novel anomalous magnetic ordering below the saturation field of the system, which is further predicted to be a Skyrmion-like ordering in CSSS. This anomaly was observed as a flat inclined region in the *M-T* curve of CSSS system at a temperature ranging from 155 K to 130 K, which appears stronger for lower *H*. This is a significant characteristic of anisotropic phase transition (T_S) with a complex magnetic order observed for CSSS crystal below the global transition temperature [20], [219], [228]–[230]. Interestingly, with lowering temperature from 130 K, *M* (ZFC) increases slowly and a broad maximum occurs near 60 K followed by a declining trend enhancing the bifurcation. This temperature is possibly attributed to the glassy transition (T_G). Such inconsistent behavior in the *M-T* curve of the CSSS system might be originated by the coexistence and completion between the ferromagnetic and anti-ferromagnetic (AFM) or spin glass (SG) states below T_C. However, under the application of higher *H*, the spins tend to orient along the applied field and the anomaly diminishes naturally. Further,

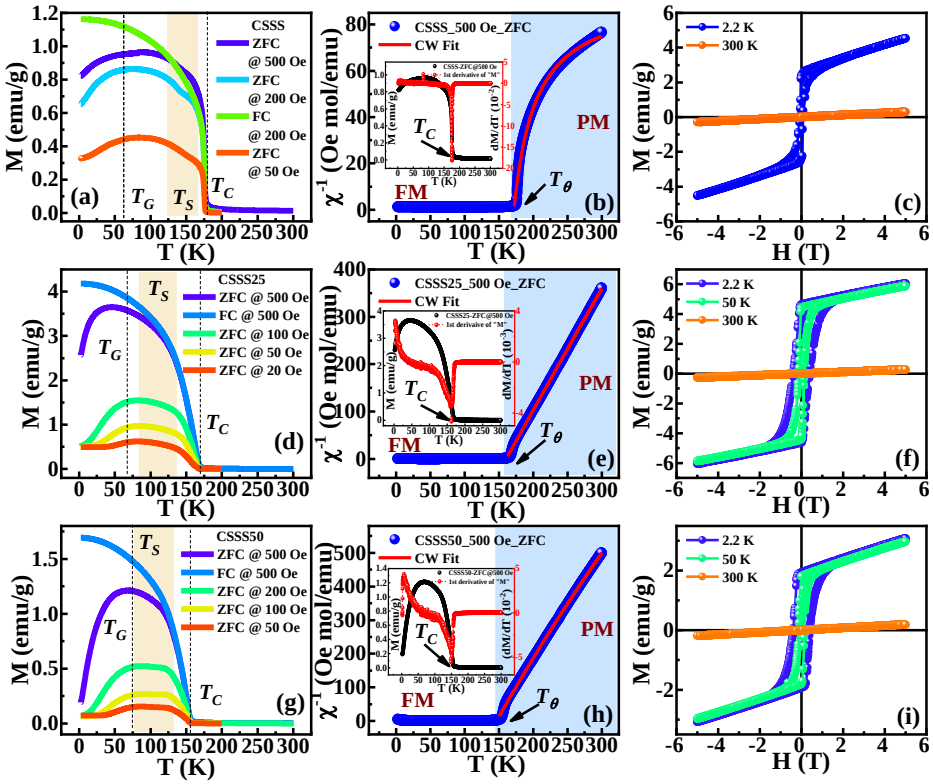

Figure 6.2: (a) Temperature-dependent magnetization curves at constant DC fields associated with CSSS. (b) Temperature-dependent inverse DC susceptibility curve fitted with CW law for CSSS. The inset shows the ZFC *M-T* and corresponding *dM/dT vs. T* curve exhibiting the transition temperature of the CSSS system. (c) Field dependency of magnetization is exhibited for CSSS at stable temperatures. (d) *M-T* curves at constant DC fields associated with CSSS25. (e) χ^{-1} *vs. T* curve fitted with CW law for CSSS25. The inset shows the ZFC *M-T* and corresponding *dM/dT vs. T* curve exhibiting the transition temperature of the CSSS25 system. (f) *M-H* curve is displayed for CSSS25 at stable temperatures. (g) *M-T* curves at constant DC fields associated with CSSS50. (h) χ^{-1} *vs. T* curve fitted with CW law for CSSS50. The inset shows the ZFC *M-T* and corresponding *dM/dT vs. T* curve exhibiting the transition temperature of the CSSS50 system. (i) *M-H* curve is displayed for CSSS50 at stable temperatures.

based on the ZFC *M-T* curve the inverse susceptibility was obtained as: $\chi^{-1}(T) = \frac{H}{M}$, and plotted against *T* to fit with the modified Curie-Weiss (CW) law as [155], [167], [228], [231],

$$\chi_0^{-1}(T) = \left(\frac{C}{T-T_\theta} + \chi_0\right)^{-1} \quad (6.1)$$

The PM region of the inverse susceptibility curve related to H = 500 Oe was fitted with CW law for CSSS as shown in Figure 6.2 (b). Here, the CW constant, C and other fitting parameters like Curie-Weiss temperature, T_θ and χ_0 are listed in Table 6.2. The effective magnetic moment (μ_{eff}) was assessed as,

$$\mu_{eff} = 2.83 \times \left(\frac{C}{\eta'}\right)^{0.5} \quad (6.2)$$

Where, η' denotes the number of magnetic atoms per unit cell, which is 3 (for 3 Co atoms) for our system. The evaluated values of μ_{eff} are also listed in Table 6.2. The *M-H* loop of CSSS at 2.2 K in Figure 6.2 (c) has a linearly increasing AFM-like trend at higher H with a robust FM loop with coercivity (H_C) around 750 Oe attributing the mixed magnetic state at such a lower temperature. At 300 K, a linear *M-H* curve with such a low magnitude is observed as the characteristic of the PM phase above T_C. Interestingly, *M-T* curves for CSSS25 (Figure 6.2 (d)) reveal that with 25% of Se doping at the S side, the magnetic moment increases approximately three times as compared to the undoped system. Thus, with increasing the doping concentration at the non-magnetic lattice site, the magnetization of the system enhances significantly. Moreover, the paramagnetic transition temperature shifts towards a lower temperature as 165.7 K, which is the minimum point of the *dM/dT vs. T* curve as shown in the inset of Figure 6.2 (e). It is noteworthy that the anomalous behavior in the *M-T* curve as described earlier occurs at a relatively lower applied field (≤ 100 Oe) and at a wider range of temperature (130 K - 85 K). Also, the modified CW formula was fitted over the paramagnetic region of the CSSS25 (Figure 6.2 (e)) and the fitting parameters are listed in Table 6.2. The *M-H* curve corresponding to CSSS25 in Figure 6.2 (f) evidences the enhancement of M as the saturation magnetization (M_S) value which is greater than the CSSS system at 2.2 K. Moreover, the coercivity of the CSSS25 is also larger than the pure system signifying the enhancement of parallel spin alignment. Further,

Figure 6.2 (g) demonstrates that by increasing the doping proportion of Se to 50 %, the shifting of T_C (the minima occurred at ~ 153.26 K shown in the *dM/dT vs. T* curve in the inset of Figure 6.2 (h)) is maintained towards the lower temperature but with a relatively lower value of magnetization as compare to the CSSS25. However, the anomalous magnetization enhances more for CSSS50 as the temperature range increases to 120 K - 80 K. All the parameters follow the regular manner by fitting the PM region of $\chi^{-1}(T)\ vs.T$ curve with the modified CW law (Figure 6.2 (h)) and tabulated in Table 6.2. It is noteworthy that T_θ < T_C for all the samples, which is insignificant considering that the reason is quantum fluctuation. However, the possible reason behind such phenomena is the competition between FM and AFM interactions below T_C. The *M-H* curve of CSSS50 in Figure 6.2 (i) matches well with the previous results and the H_C is ~ 4000 Oe. Thus, observing the unusual rise and fall in the *M-T* curves we predicted an unconventional magnetic phase in our present system at a particular range of temperature and field and shaded the region with yellow color in Figure 6.2 (a, d, g) correspondingly for CSSS, CSSS25 and CSSS50. Noticeably, the range of the new unconventional magnetic phase enhances with raising the doping concentration of Se in our system.

Table 6.2 Parameters determined from the CW equation fitted over the χ^{-1} vs T ZFC data at 500 Oe applied field and the M-H curves corresponding to CSSS, CSSS25 and CSSS50 systems.

Parameters	**CSSS**	**CSSS25**	**CSSS50**
T_C (K)	176.51	165.70	153.26
T_Θ (K)	171.83	160.55	146.38
C (emu K/mol)	0.342	0.382	0.276
χ_0 (10^{-3} Oe mol/emu)	10.68	4.57	2.05
μ_{eff}	1.0739	1.0099	0.8584
H_C (Oe)	750	3950	4000
M_S (emu/g)	2.40	4.63	1.93

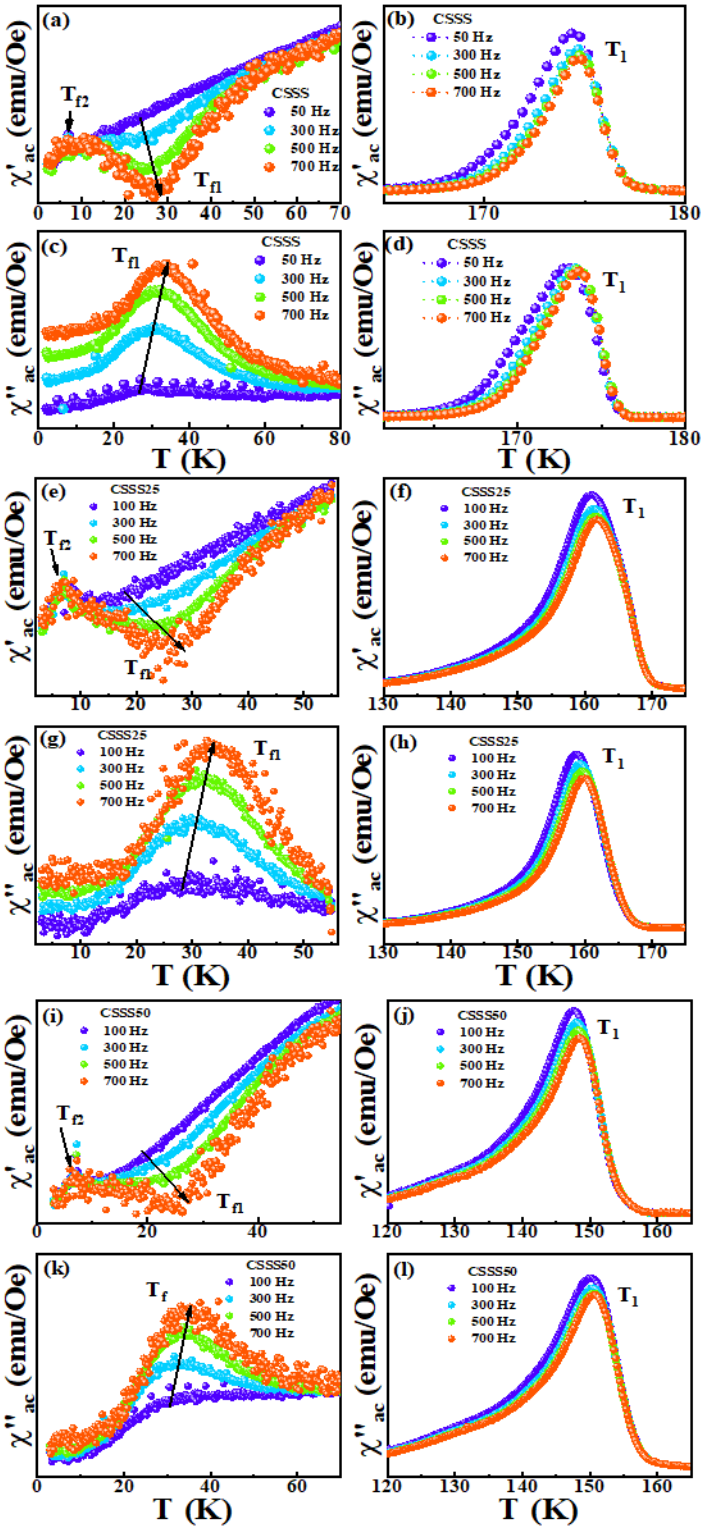

Figure 6.3: (a), (b) Exhibit frequency dependency on $\chi'_{ac}(T)$ and (c), (d) display $\chi''_{ac}(T)$ curves at different frequencies associated with CSSS. (e), (f) Demonstrate frequency dependency on $\chi'_{ac}(T)$ and (g), (h) show $\chi''_{ac}(T)$ curves at different frequencies associated to CSSS25. (i), (j) Exhibit $\chi'_{ac}(T)$ curves at different constant frequencies and (k), (l) present $\chi''_{ac}(T)$ curves at diverse frequencies for CSSS50.

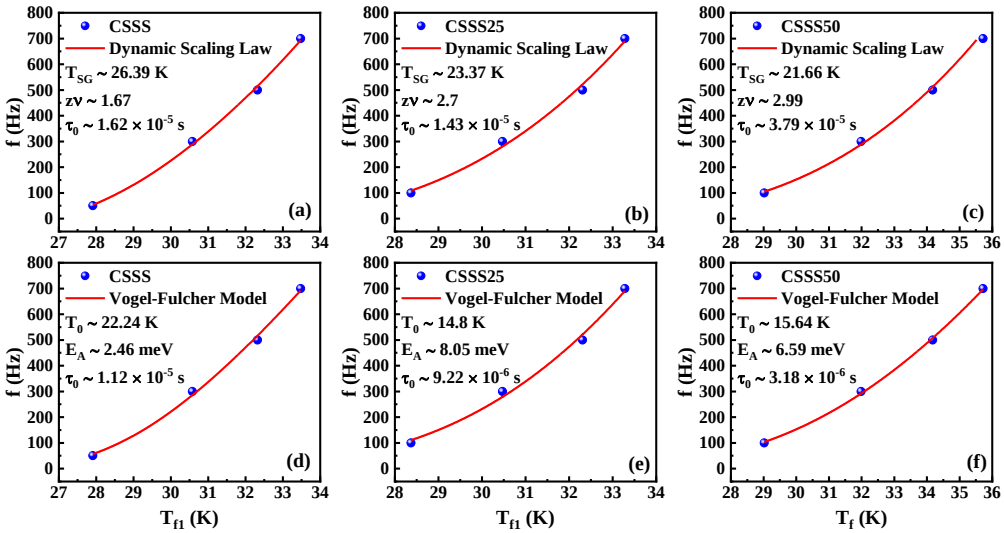

Figure 6.4: Dynamic Scaling law fitted freezing temperature versus frequency curves corresponding to (a) CSSS, (b) CSSS25 and (c) CSSS50 are presented. (d), (e) and (f) exhibit f vs T_{f1} curves following the Vogel-Fulcher model respectively for CSSS, CSSS25 and CSSS50.

To further examine the novel anomalous magnetic phase in our system we accomplished the in-phase as a real part (χ'_{ac}) and out-of-phase component as an imaginary part (χ''_{ac}) of AC susceptibility measurements on our system concerning temperature at different frequencies (Figure 6.3) and at the different applied magnetic fields (Figure 5). Figure 6.3 (a, b) and Figure 6.3 (c, d) show the temperature dependence of χ'_{ac} and χ''_{ac} at different frequencies (50 – 700 Hz) applying a constant AC field of 3 Oe in absence of any DC bias with the intention of probing the response of the system against perturbation for CSSS system. Variation of the χ'_{ac} with the temperature shows an anomaly at T_{f1} ~ 21.56 K (freezing temperature) (shown in Figure 6.3 (a) below T_G) and a sharp peak at T_1 ~ 174.39 K (shown in Figure 6.3 (b) just below T_C) for f ~ 50 Hz exhibiting distinct frequency-dependency. Also, the χ''_{ac} *vs.* T curves (Figure 6.3 (c, d)) exhibit similar anomaly and frequency dependency with a significant shifting in the freezing temperature at 27.91 K and 172.85 K (at f = 50 Hz). It is evident that with increasing frequency, there is a shift in both the peak position towards higher temperatures. Such shifting is caused by the

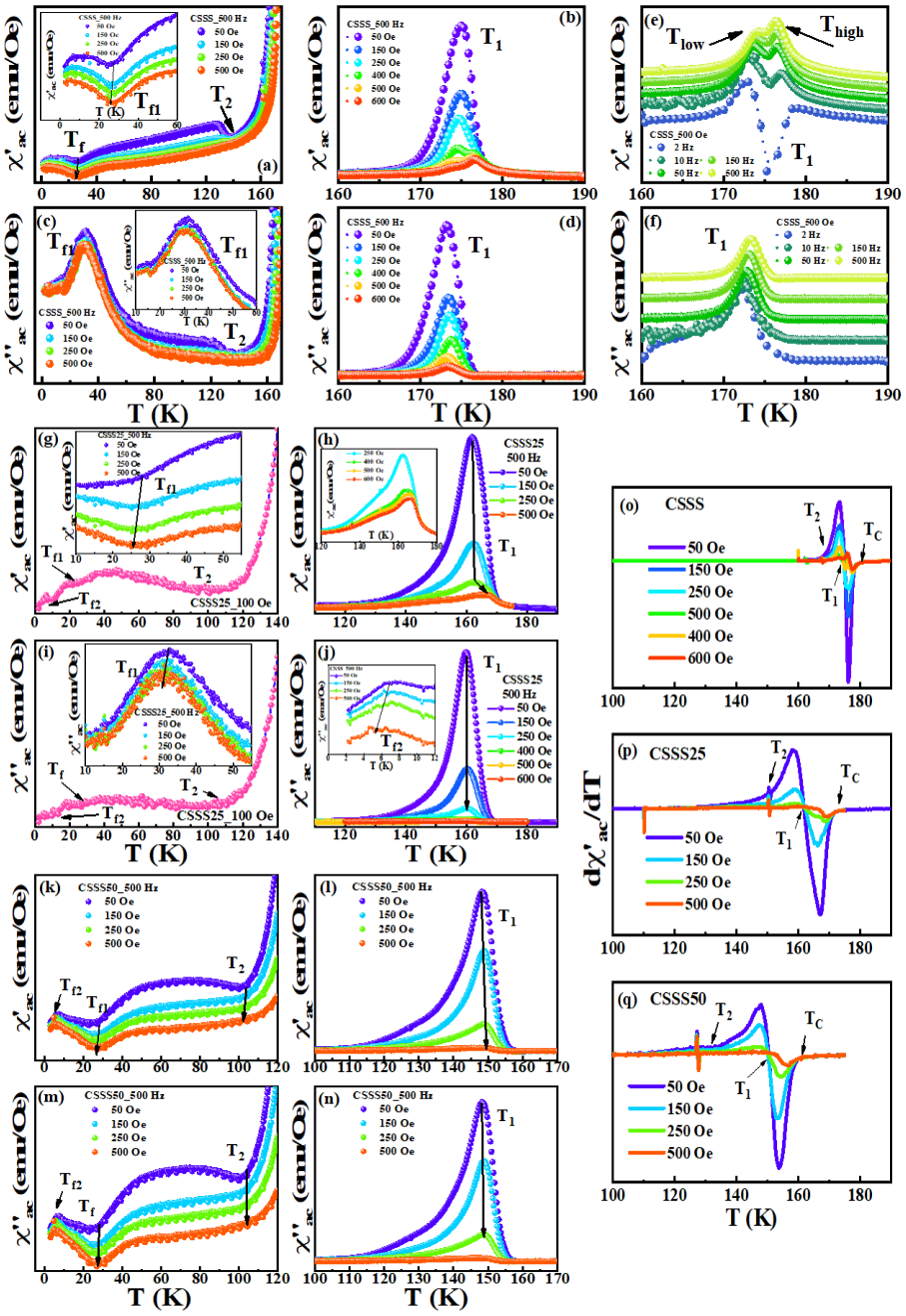

Figure 6.5: (a), (b) Exhibit field dependency on $\chi'_{ac}(T)$ with an inset containing the closer view of χ'_{ac} *vs. T* below the freezing temperature at different DC bias of CSSS at constant frequency 500 Hz. (c), (d) Display $\chi''_{ac}(T)$ curves at different constant DC fields associated with CSSS with an inset inclosing the larger view of χ''_{ac} *vs. T* below freezing temperature varying fields. (e), (f) Exhibit the frequency dependency on $\chi'_{ac}(T)$ and $\chi''_{ac}(T)$ respectively at constant DC bias 500 Oe. (g), (h) Demonstrate DC applied field dependency on $\chi'_{ac}(T)$ and (i), (j) show $\chi''_{ac}(T)$ curves varying fields associated to CSSS25. The inset of (g) and (i) display the larger view of the respective curves below the glassy transition. The inset of (h) shows $\chi'_{ac}(T)$ at additional fields. The inset of (j) exhibits $\chi'_{ac}(T)$ at various fields adjacent to T_{f2}. (k), (l) Exhibit $\chi'_{ac}(T)$ curves and (m), (n) present $\chi''_{ac}(T)$ curves at different DC fields associated to CSSS50. (o), (p) and (q) Displays the $d\chi'_{ac}/dT$ with respect to *T* corresponding to CSSS, CSSS25 and CSSS50, respectively.

prolongation of the action time-induced spin relaxation delay. Also, the magnitude of the peak reduces with an increase in the frequency of the applied excitation wave at both peak positions. This tendency defines the existence of the spin-glass-like behavior of the compound below T_G. So, to recognize the specific compound among different glassy states, we evaluated the Mydosh parameter (P) investigating the relative peak shift at T_{f1} with respect to frequency. For the spin-glass or cluster glass (CG) state, the magnetic entities interact weakly; hence, acquiring very high sensitivity and the Mydosh parameter is a measure of the sensitivity to the applied frequency. Thus, in order to understand the spin dynamics of the compound the Mydosh parameter can be expressed as [232]–[234],

$$P = \frac{\Delta T_f}{T_{f1}\Delta log_{10}(f)} \tag{6.3}$$

Where, $\Delta log_{10}(f) = log_{10}(f_2) - log_{10}(f_1)$ and $\Delta Tf = (Tf_2) - (Tf_1)$. For CSSS, we calculated P as 0.095, which signifies the system falls under the cluster glass state ($0.07 < P < 0.2$) below T_G ruling out the existence of a super-paramagnetic state ($P > 0.2$) [235]–[237]. Such a glassy transition occurred at T_{f1} as a consequence of the geometrically frustrated triangular magnetic Co chains in the Kagome structure of the CSSS system. In addition, the sharp peak in $\chi'_{ac}(T)$ (Figure 6.3 (b)) and χ''_{ac}(T) (Figure 6.3 (d)) just below T_C appeared originally due to the global phase transition from PM to FM state. CSSS25 (Figure 6.3 (e-h)) and CSSS50 (Figure 6.3 (i-l)) also exhibit similar phenomena while investigating the temperature-dependent AC susceptibility varying frequency. Both the peaks corresponding to T_{f1} and T_1 in $\chi'_{ac}(T)$ shift toward lower temperature with increasing doping concentration of Se as shown in Figure 6.3 (a, b, e, f, i, j) which signifies the previous results of *M-T* curves (Figure 6.2 (a, d, g)) with decreasing trend of the transition temperature. The Mydosh parameter was evaluated as 0.111 and 0.157 at f = 100 Hz below T_G for CSSS25 and CSSS50, respectively. Eventually, the value of P lies in the range of cluster-glass state

for both the Se-doped systems. However, numerically the *P* value raises consistently with enhancing Se concentration signifying that the FM ordering is dominating over the AFM for higher Se concentration at the frustrated state. This is also consistent with the *M(T, H)* curves in Figure 6.2, as the numerical value of magnetization and coercivity is higher for the doped samples as compared to the undoped CSSS suggesting the dominance of the ferromagnetic behavior. Eventually, to establish the phenomenon related to the deceleration of spin dynamics in a glassy state below freezing temperature, we inspected the dynamic scaling law as [238]–[241],

$$f = f_0 \left(\frac{T_f - T_{SG}}{T_{SG}}\right)^{zv} \tag{6.4}$$

Where, T_f signifies the temperature attaining the maximum $\chi'_{ac}(T)$ at frequency *f*, T_{SG} refers to the equivalent SG freezing temperature without application of frequency and DC field. f_0 is associated with the characteristic spin flipping time as; $\tau_0 = \frac{1}{f_0}$ and *zv* signifies the dynamical critical exponent. We fitted the T_{f1} *vs. f* data points with the dynamic scaling (Shown in Figure 6.4 (a-c)) equation yielding the spin-flip time at the range of 10^{-5} seconds and *zv* was evaluated as 1.67, 2.7 and 2.99 (satisfactory value for a typical glassy state) for CSSS, CSSS25 and CSSS50, respectively [239], [242], [243]. τ_0 attributes the value as small as 10^{-12} s to 10^{-13} s for the canonical SG system. However, for our system, the value is significantly high indicating the freezing of magnetic clusters of finite size, which requires more time to relax with respect to individual spins [166], [238], [242], [244]. Further, Figure 6.4 (d-f) displays the dependence of freezing temperature on frequency to investigate the inter-cluster interaction employing the empirical Vogel-Fulcher law [238], [239],

$$f = f_0 exp\left(\frac{-E_A}{K_B(T_f - T_0)}\right) \tag{6.5}$$

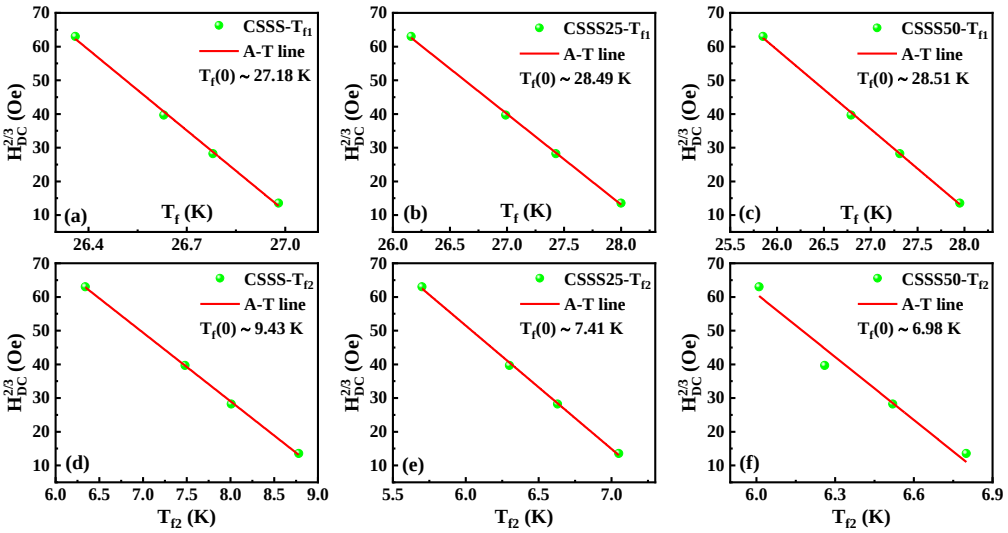

Figure 6.6: DC field dependency on freezing temperature fitted with Almeida - Thouless line for (a) CSSS, (b) CSSS25 and (c) CSSS50 are presented at T_{f1} whereas (d), (e) and (f) exhibits the same at T_{f2} for CSSS, CSSS25 and CSSS50, respectively.

Here, T_0 denotes the interaction strength among clusters and E_A corresponds to the activation energy. f_0, T_f, K_B follow usual notations. The obtained values of all the parameters designate the existence of strong inter-cluster interaction in the system. τ_0 values (10^{-5}-10^{-6}) are comparable to the range exhibited earlier from the dynamic scaling law and strongly suggest the existence of a CG system instead of a canonical SG state below T_{f1} [238], [239]. Other than these two global (T_1) and local (T_{f1}) transitions, the present system exhibits another local transition adjacent to 8 K. We have denoted the temperature as T_{f2} in Figure 6.3 (a, e, i) where the anomaly occurred in $\chi'_{ac}(T)$. A broad transition at such a low temperature might be associated to the second glassy phase possibly due to spin frustrations, though the reason behind the double glassy state is not much clear from the frequency-dependent study of the present system. In our next section we have tried to enlighten the explanations behind the second glassy transition that occurred at such a low temperature by studying field dependency of the $\chi'_{ac}(T)$ and $\chi''_{ac}(T)$.

Additionally, in order to inspect the unconventional magnetic phase, we performed $\chi'_{ac}(T)$ and $\chi''_{ac}(T)$ measurements varying the DC applied field from 50 Oe to 600 Oe and exhibited in Figure 6.5 (a-f), Figure 6.5 (g-j) and Figure 6.5 (k-n) consistently for CSSS, CSSS25 and CSS50 systems. Interestingly, pure CSSS exhibits anomaly at four temperature regions in both temperature-dependent in-phase and out-of-phase AC susceptibility curves (Figure 6.5 (a-f)). Among the four regions, we have already discussed three previously. At 50 Oe applied magnetic field and 500 Hz frequency, the first maxima happened at T_1 (175 K) just below T_C due to the global transition occurring from PM to FM. The second and third anomaly located at T_{f1} (25.55 K) and T_{f2} (8.1 K) below the glassy transition temperature, T_G due to some local magnetic alignments correlated to the spin frustration. The peaks associated with T_{f1} and T_{f2} display some shift towards lower temperature with applying a higher DC field indicating an entirely different kind of magnetic ordering modulated by very small DC bias. Here, T_{f1} signifies a cluster-glass transition as described earlier by frequency dependency of the AC susceptibility components. However, for T_{f2}, the peak is suppressed and the peak temperature is shifted towards a lower temperature with an application of the DC magnetic field, which signifies a typical spin-glass state. Fascinatingly, a fourth anomaly was discovered with a broad peak near 128.52 K and a valley adjacent to 138.81 K at H = 50 Oe and f = 500 Hz for CSSS and the valley temperature is denoted as T_2 in Figure 6.5 (a, c). Such anomalous nature was observed previously in pure CSSS systems [20], [76]. With further increment in the applied field, the anomaly shifts toward lower temperature and diminishes slowly at 150 Oe and 250 Oe. Noticeably, the anomalous nature almost disappears at H = 500 Oe in both $\chi'_{ac}(T)$ (Figure 6.5 (a)) and $\chi''_{ac}(T)$ (Figure 6.5 (c)) curves. This nature is consistent with the anomaly (region T_S) observed in the ZFC M-T curves of the CSSS system. Here also, the anomaly reduces and shifts toward the lower temperature side with applying further field

and nearly disappears at 500 Oe. Such an anomaly at a lower DC field (< 500 Oe) indicates the possibility to develop a new anomalous magnetic ordering apart from the conventional FM state between T_1 and T_{f1}. More interestingly, for pure CSSS system the peak at T_1 is suppressed, broadened, and split into two maxima with the application of higher DC bias as shown in Figure 6.5 (b). The peak, which is at the higher temperature (T_{high}) shifts towards the higher temperature side on increasing the applied field gradually. Noticeably, similar thermal deviation in T_C concerning the higher temperature was demonstrated by the *M-T* curves (Figure 6.2 (a)) with an application of higher *H*. This is consistent with the peak shift associated to the T_{high} with the externally applied DC magnetic field. Such a phenomenon is familiar to the manifestation of critical fluctuations accompanying a continuous transition to an FM state. Remarkably, the peak associated with the lower temperature (T_{low}) moves towards the lower temperature side with the enhancement of the applied field. Though $\chi'_{ac}(T)$ is anticipated to be constant below T_C, the coexistence of the FM and AFM clusters of finite size might be the reason behind such dislocation of T_{low} peak tends to lower temperature. This phenomenon is recognized as the Hopkinson effect associated with magnetic anisotropy/inhomogeneity. The magnetic anisotropy modifies with decreasing temperature owing to incessant transformation in size and shape of FM clusters below T_C [155], [245], [246]. The fascinating Hopkinson effect is recognized by the competing spin-spin correlations and comparably larger anisotropy field. This effect can be designated by the relation [155], [247]:

$$\chi'(T)\ \alpha\ \frac{M_S^2(T)}{K(T)} \tag{6.6}$$

In this equation, $M_S(T)$ denotes spontaneous magnetization, whereas $K(T)$ signifies the anisotropy energy at a particular temperature. If we consider a temperature just below T_C, due to the strong ferromagnetic spin-spin correlations, spontaneous magnetization is almost

constant. Henceforth, the reduction in $\chi'_{ac}(T)$ with the enhancement of the magnetic field should be associated with a simultaneous increase in $K(T)$. Possibly, this enhancement in anisotropic energy is initiated by the local magnetic frustration between the ferromagnetically and anti-ferromagnetically aligned spins. Thus, an additional peak is being demonstrated just below T_C driven by the large anisotropy energy, as it blocks the spin and prohibits responding under magnetic field and is designated as Hopkinson peak. Such upsurge in the anisotropy energy below T_C is modulated by incessant modifications in the magnitude and shape of the FM cluster initiated by the domain wall motion [242], [246]. Interestingly, both the real and imaginary part of AC susceptibility exhibits thermal discrepancy with varying frequency at a constant AC field (3 Oe) and DC bias (500 Oe). Figure 6.5 (c) displays that the peak corresponding to T_{low} in $\chi'_{ac}(T)$ stimulates slightly and consistently shifts towards the lower temperature side with lowering frequency. However, the spins have a general tendency to follow a smaller frequency. This is the reason behind the relative enhancement of the peak corresponding to T_{low} with decreasing frequency. Therefore, the splitting of the peaks at relatively higher DC bias and lower frequency might be due to a slow spin relaxation. In contrast, the origin of the peak corresponding to T_{high} is probably due to the long-range ordering adjacent to the magnetic transition temperature. Therefore, the relative height of this peak suppresses simultaneously with a constant but insignificantly small shift along higher temperatures with a decrement in frequency. In addition, Figure 6.5 (f) demonstrates the thermal variation of $\chi''_{ac}(T)$ peak towards lower temperature with decreasing frequency evidencing the slow spin relaxation phenomena. Now, with Se doping the development and modification of the new magnetic phase adjacent to T_2 is a matter of interest in our system. When we observed $\chi'_{ac}(T)$ (Figure 6.5 (g, h)) and $\chi''_{ac}(T)$ (Figure 6.5 (i, j)) for CSSS25 and $\chi'_{ac}(T)$ (Figure 6.5 (k, l)) and $\chi''_{ac}(T)$ (Figure 6.5 (m, n)) for CSSS50, we witnessed similar magnetic transitions as discussed

earlier for the pure system. Unlikely the frequency-dependent study, the cluster-glass transition temperature (T_{f1}) is approximately constant at the fixed fields (H = 50, 150, 250, 500 Oe) and frequency (500 Hz) for all three samples. Nevertheless, with increasing DC bias, the peak corresponding to T_{f1} moves toward a lower temperature. This phenomenon is identical to the second glassy state adjacent to T_{f2}, displayed in the inset of Figure 6.5 (j). Typical SG or CG systems exhibiting the downward tendency of the freezing temperature concerning the DC field eventually get smeared out with a sufficiently large field owing to domain wall relaxation. In consequence, we fitted the Almeida-Thouless (A-T) line on the $H^{2/3}{}_{DC}$ *vs.* T_f *(H)* data points using the equation [239],

$$H_{DC}^{2/3} = \Delta J^{2/3}\left[1 - \frac{T_f(H)}{T_f(0)}\right] \tag{6.7}$$

Where, ΔJ is a proportion constant and $T_f(H)$, $T_f(0)$ correspond to the freezing temperatures with and without application of DC bias. The well-fitted data in Figure 6.6 (a-c) signifies the CG transition below T_{f1} and Figure 6.6 (d-f) suggests the existence of the SG phase below T_{f2}. The A-T line is basically evidencing the existence of random anisotropy which is a reason behind the initiation of such glassy transitions [248]. Even a small anisotropy may create double glassy transitions since both phases are consistent with the A-T line model corresponding to the Heisenberg system [248]. However, the $T_f(0)$ adjacent to the first glassy state T_{f1} is significantly identical to the experimental observation and nearly constant with varying doping concentrations suggesting the cluster formation below T_{f1}. Whereas, the second glassy transition at the vicinity of T_{f2} varies toward lower temperatures with higher doping concentration as displayed in Figure 6.6 (d-f). And, the higher values of the proportion constant corresponding to the second glassy transition implies the randomness in the system due to spin frustration only [238]. Thus, the transition below T_{f2} signifies the canonical SG magnetic frustrated state. This field-dependent nature

differentiates the present system from the characteristic geometrically frustrated systems exhibiting dual glassy transition owing to deformation. Somewhat, it introduces a field-dependent remarkable magnetic phase like Skyrmions. However, the peak due to the global transition adjacent to T_1 is consistently decreasing to lower temperature with the Se doping concentration following the DC magnetization curve with respect to temperature as shown in Figure 6.2 (d, g). Also, with the application of a higher field, the peak suppression and broadening happen following a similar manner as CSSS. Nonetheless, the peak splitting and slow spin relaxation were quite unclear at the higher field for higher doping systems. Excitingly, the anomaly associated with T_2 also systematically decays toward lower temperatures with increasing doping concentration. Finally, For TSSS50, the broad anomaly occurs near T_2 = 101.65 K, which is a far lower temperature in comparison to T_2 (138.81 K) for CSSS and this region has a perceptible field dependency evidencing a relatively lower suppression field. This thermal reduction of the enormous magnetic phase associated with T_2 is also clearly exhibited in Figure 6.5 (o, p, q) with the temperature dependency of the $d\chi'_{ac}/dT$ corresponding to CSSS, CSSS25 and CSSS50, respectively. Interestingly, this systematic reduction of the transition temperatures T_1 and T_2 follow quite similar nature observed with the application of pressure [76]. Previously, some researchers have successfully evidenced nearly 10 K shifting of both T_1 and T_2 concerning lower temperature under 11.26 Kbar pressure regarding the ambient condition [76]. In comparison to that, we have observed a nearly 25 K deviation in the global transition temperature to the lower side by replacing 50% S atoms with relatively heavier Se atoms in CSSS50. Moreover, the transition temperature related to the newly studied phase exotically deviated approximately 37 K (for the CSSS50) to the lower temperature side which is huge in comparison to the external pressure effect described above. The interstitial disorders related to the introduction of larger atoms are possibly producing a chemical

pressure on the system, which is affecting even harder than the physically applied pressure of the range of a few Kbars. Additionally, the phase is mostly disappearing above 250 Oe for CSSS50, which is much lower than the vanishing field associated with the pure system (500 Oe). This reduction in the anomalous magnetic phase region is also evidencing the effect of pressure, which is due to the chemical tension in our system. The pressure-induced volume modification and the fluctuations in the Co-Co interlayer interactions in the Kagome layer might be the reason behind the reduction of the anomalous phase space (*H-T*). However, in our system, the anomalous region is broadening with increasing the Se concentration and the phenomena are observable at a relatively lower field. In accordance with the Bak-Jensen model [62], [63], [249], the propagation vector, k_s is well-defined by the ratio; $k_s = \frac{D}{J}$, where *D* signifies the DMI constant and *J* is associated with the isotropic Heisenberg exchange constant. Subsequently $T_C \propto J$, thus the magnitude of *D* might be determined by T_C and k_s for a respective system. Replacing S with larger Se atoms at the nonmagnetic site may contribute to a diverse *D/J* ratio. The k_s value is reportedly modified by the chemical substitution of magnetic/nonmagnetic atoms at the magnetic atom site; hence, enhancement/suppression of the Skyrmion stability was noticeably adapted with the DMI [63]. In addition, the Skyrmion stability is comparable to the DMI constant. However, the development of the Skyrmion stability may not only depend on DMI but also may be adapted by cubic anisotropy [250], [251]. Previously, investigation of the low defect concentration with constant DMI led to a significantly long-range modification to the spiral period [252]. Therefore, we can predict that the local defects in DMI associated with the spin frustration may change the periodicity of the whirl-like structure in the system instead of occurring local distortions. However, in order to evaluate the temperature dependence of the above-mentioned anisotropy, we manifested the law of approach (LA) to the first

quadrant of the *M-H* curves corresponding to all compositions at the saturation region basically above the coercivity field as [253],

$$M = M_S\left[1 - \frac{8}{105\mu_0^2 M_S^2}\left(\frac{k_1}{H}\right)^2\right] + kH \tag{6.8}$$

As for conventional FM, the hysteresis loop closes with the completion of all the irreversible spin ordering, further increase in *M* with the application of a higher field indicates the rotational processes associated with the magnetic anisotropy. Thus, at the saturation region, the LA model fits well on the system varying the Se concentration as shown in Figure 6.7 (a). the numerical coefficient 8/105 is related to cubic anisotropy. k_1 signifies the cubic anisotropy constant and *kH* indicates the forced magnetization with the enhancement of the spontaneous *M* at a higher field region. k is the high field susceptibility and M_S is the saturation magnetization. With the best-fitted LA equation, we obtained the parameters M_S as 2.68, 4.72, 1.99 emu/g and k_1 as 1.303 × 10^4, 2.062 × 10^4, 1.278 × 10^4 J/m^3 for CSSS, CSSS25 and CSSS50 respectively at the lowest measured temperature 2.2 K. Interestingly, the parameters are exhibiting highest values for the 25% Se doped sample indicating the development of the strong FM ordering with maximum anisotropy initiated by the Se substitution at S site. But, by increasing the doping concentration to 50%, the

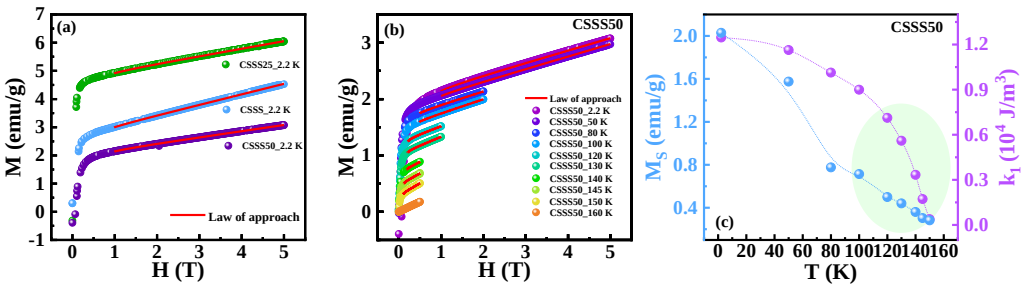

Figure 6.7: (a) the First quadrant of the *M-H* curves fitted with the law of approach model for CSSS, CSSS25 and CSSS50 at the lowest temperature 2.2 K. (b) law of approach model fitted on the *M-H* curves of CSSS50 at the entire range of temperatures below T_C. (c) Temperature dependency of the saturation magnetization and cubic anisotropic constant for CSSS50.

anisotropy diminishes developing additional disorder in the system. However, the magnetic AC susceptibility displays anomaly at the maximum temperature range for CSSS50 among the present systems. So, we further inspected the isothermal *M-H* curves of the 50% Se doped system with the LA model at a wide range of temperatures below T_C as shown in Figure 6.7 (b). The attained saturation magnetizations and the cubic anisotropy constants are exhibited in Figure 6.7 (c). Both of them follow a downturn behavior with a consistent upsurge of temperature. Conspicuously, both the M_S and k_1 parameters demonstrate a certain anomaly at the vicinity of 100 K, which is definitely very close to the anomalous transition temperature T_2. The shaded region in Figure 6.7 (c) is essentially predicted to be exhibiting a Skyrmion-like complex magnetic phase from the field dependent $\chi'_{ac}(T)$ and $\chi''_{ac}(T)$ study. The dynamic temperature dependence of the cubic anisotropic constant evaluated by the LA model signifies that the change in anisotropy might be a probable reason behind the observed exotic magnetic phase. Also, the anisotropy significantly reduces for the system with the highest doping concentration for which the Skyrmion stability is evidently elongated. Such local modifications in the cubic anisotropy possibly influence the magnetic texture enhancing the stability of the Skyrmions owing to the chemical substitution. The puzzling phenomenon observed in the new exotic magnetic phase space in our system considerably evidences that to be the Skyrmion-like phase. As the Kagome ferromagnet CSSS, composed of corner-sharing Co atoms proved to be exhibiting a geometrically spin-frustrated cluster-like state at low temperatures, the complex magnetic interactions were initiated by the application of a very small magnetic field. However, at a particular temperature range, these interactions develop multiple magnetic phases introducing twisted particle-like spin arrangements named Skyrmions. Thus, a robust non-colinear low-field anomalous magnetism was demonstrated by introducing chemical pressure in a Kagome FM.

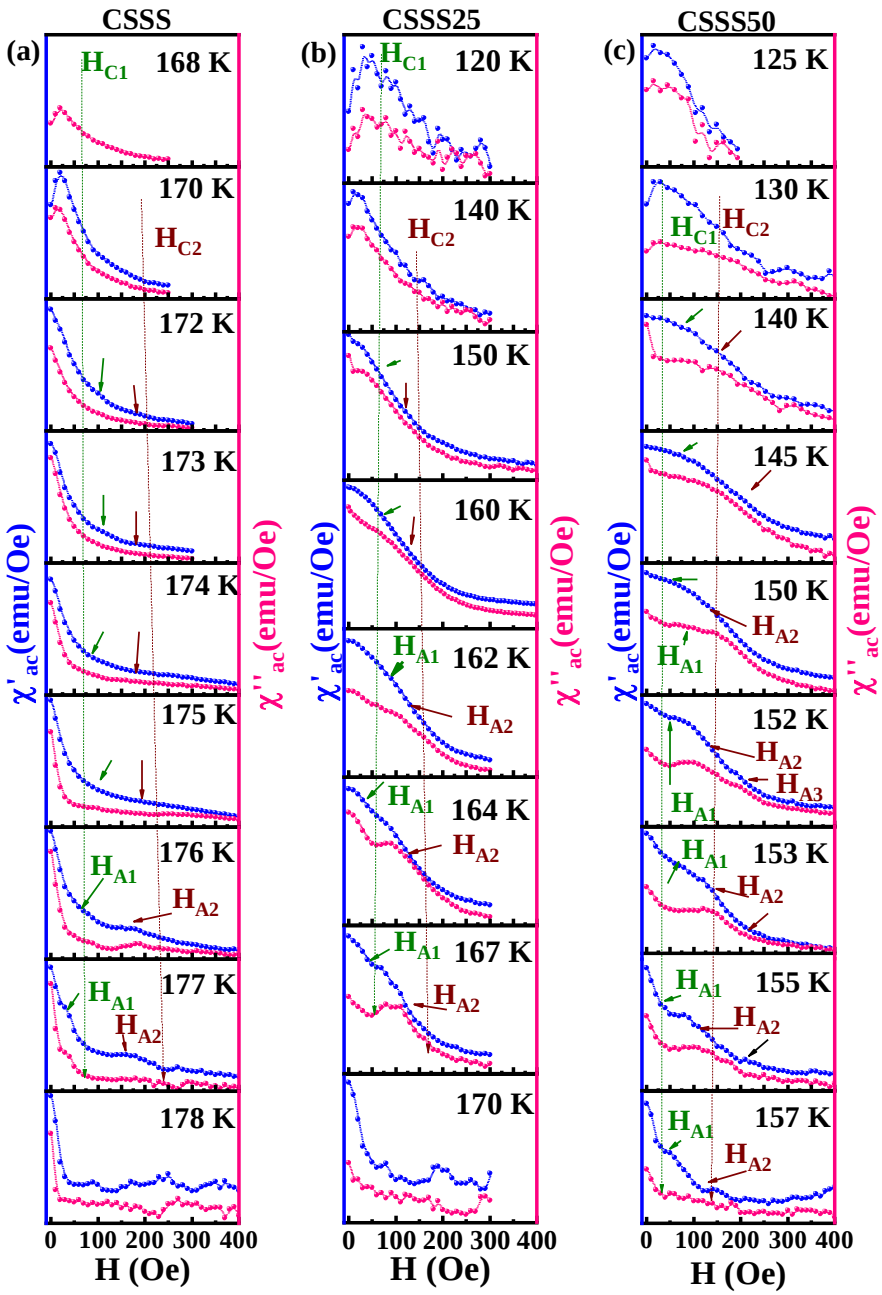

Figure 6.8: (a) Displays $\chi'_{ac}(H)$ and $\chi''_{ac}(H)$ curves at different temperatures exhibiting diverse magnetic phase boundaries at very low DC applied field for CSSS. (b) Displays $\chi'_{ac}(H)$ and $\chi''_{ac}(H)$ curves varying temperatures corresponding to CSSS25. (c) Displays temperature dependency on $\chi'_{ac}(H)$ and $\chi''_{ac}(H)$ curves exhibiting unusual magnetic phase boundaries at very low field.

In order to identify the modification of the Skyrmion phase by introducing the chemical pressure in a pure $Co_3Sn_2S_2$ system, we measured both in-phase ($\chi'_{ac}(H)$) and out-of-phase ($\chi''_{ac}(H)$) components of isothermal AC susceptibility varying applied field under an altering current modulation field of 3 Oe and frequency 10 Hz. All the measurements were carried out in the ZFC mode eliminating the history related to past H and T dependency and the accumulated results are displayed in Figure 6.8 (a, b, c) for CSSS, CSSS25 and CSSS50, respectively. In all three systems, several distinct phase boundaries are observed with the application of small perturbation and designated in Figure 6.8 as some cut of fields (H_{C1}, H_{C2}) and anomalies (H_{A1}, H_{A2}). The presence of a noticeable characteristic peak/dip kind of anomaly in the $\chi'_{ac}(H)$ and $\chi''_{ac}(H)$ curves suggests that the applied DC magnetic fields gradually transform the system into different magnetically ordered states predicting prominent Skyrmion-like magnetic phase. We can specify the Skyrmion phase space deducing the narrow field region as $\Delta H = H_{A1} - H_{A2}$ at the range of temperature $\Delta T = T_{A1} - T_{A2}$ (T_{A1} and T_{A2} are respectively the lowest and highest temperatures where the Skyrmion-like ordering is observed for each sample). Figure 6.8 (a) displays isothermal $\chi'_{ac}(H)$ and $\chi''_{ac}(H)$ characteristics of pure CSSS system at temperatures ranging from 168 K to 178 K under the application of small variable field 0 to 400 Oe. The existence of distinct anomalies in $\chi'_{ac}(H)$ and $\chi''_{ac}(H)$ curves of the CSSS system was observed at temperatures ranging from 172 K to 177 K. Thus, the Skyrmionic temperature region ΔT is approximately 5 K and the field region ΔH is nearly 120 Oe for the pure system. Whereas for CSSS25, the complex magnetic ordering was induced at a broader range of temperature from 150 K to 167 K (Figure 6.8 (b)) exhibiting $\Delta T \sim 17$ K and $\Delta H \sim 150$ Oe. This expansion of the Skyrmionic phase was sustained for the CSSS50 system also, where the anomalous temperature range was observed from 130 K to 157 K ($\Delta T \sim 27$ K and $\Delta H \sim 150$ Oe.) as shown in Figure 6.8 (c). Such a systematic increase in the Skyrimionic phase space was

observed previously for different oxide and non-oxide Skyrmionic non-centrosymmetric heli-magnets under the application of physical pressure of few GPa [16], [230], [254]. In our system, comparatively bigger Se atoms are playing an important role introducing chemical pressure inside the Kagome ferromagnet. As a result of the strain developed inside the non-centrosymmetric arrangements of Kagome magnets, the spins are modified conveniently to demonstrate Skyrmionic phenomena at a bigger phase space with a higher doping concentration of Se. Here we present the magnetic phase diagrams of CSSS, CSSS25 and CSSS50 based on the magnetization ($M(H, T)$) and temperature and field dependent ac susceptibility ($\chi'_{ac}(T, H)$ and $\chi''_{ac}(T, H)$) data described above. Figure 6.6 (a, b, c) illustrates the *H-T* phase diagram corresponding to CSSS, CSSS25 and CSSS50 crystals, where T_C (T_1), T_{f1} and T_2 were determined by analyzing the temperature dependency of magnetization and ZFC AC susceptibility at a different frequency and magnetic field and we predicted a Skyrmion-like fascinating spin texture in our system somewhere in between T_C and T_2. Further, investigating the low-field dependency of AC susceptibility we were able to specify the Skyrmion phase space (ΔH-ΔT) signifying that the desired phase is characterized by a nontrivial spin texture prior to a field-stabilized collinear ferromagnetic structure. In accordance with the prior investigations of our system in this article, we have denoted different magnetic regions as FM_1, FM_2 and FM_3 summarizing them in the *H-T* phase diagrams. The non-magnetic region is denoted as PM, and the spin-frustrated cluster-glass region below the freezing temperature is symbolized as CG. The *H-T* region enclosed by H_{A1}, H_{A2}, T_{A1} and T_{A2} is denoted as the S phase in Figure 6.9 (a, b, c). This inconsistent magnetic phase is situated above the anomalous temperature T_2 and just below the transition temperature T_C surrounded by dissimilar magnetic states (PM, FM_1, FM_2 and FM_3). The whirl-like Skyrmionic phase in the Sk region basically originated from the neighboring diverse spin alignments. Fascinatingly, the Skyrmionic

phase space is expanding and intensifying with a higher doping concentration of Se replacing smaller Sk atoms. This expansion is vibrantly noticeable in the phase diagrams of Figure 6.9. The systematic improvement of ΔT and ΔH region is clearly visible from the undoped to 50% Se doped system. However, the absolute value of critical temperature and critical field corresponding to the Skyrmionic phase is lowering consistently with increasing Se concentration. This phenomenon signifies that by enhancing chemical pressure in the system, we can achieve the complex magnetic Skyrmionic phase with applying a comparatively lower field. This is an amusement to accomplish Skyrmionic texture at such a low field as 100 Oe at ambient pressure in presence of chemically persuaded tension.

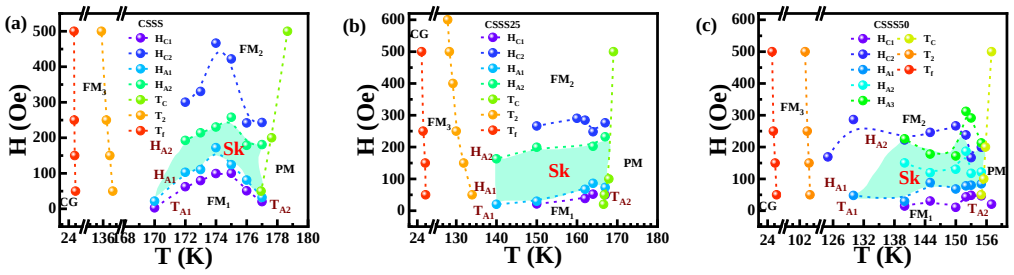

Figure 6.9: *H-T* phase diagrams are demonstrated in (a), (b) and (c) associated with CSSS, CSSS25 and CSSS50, respectively.

6.4 Conclusions and Prospects

In order to inspect the structural purity of the as-prepared $Co_3Sn_2S_{2(1-x)}Se_{2x}$ system, we scrutinized the powder XRD data corresponding to all the samples and confirmed the rhombohedral shandite structure with $R\bar{3}m$ *(166)* space group. The expanded volume of the unit cell with growing Se concentration replacing the S site generates an interstitial defect in the crystal structure and produces chemical strain inside the unit cell. The geometrically frustrated Co atoms sharing the corners of the triangle of each Kagome ferromagnetic unit form trigonal anti-prismatic configurations in the Kagome layer. This kind of frustration between FM and AFM type spin alignments further initiates a magnetic

transition associated with the cluster glass phase below the freezing temperature corresponding to each sample and manifested by ZFC *M-T* curves following field and frequency deviated $\chi'_{ac}(T)$ and $\chi''_{ac}(T)$ measurements. Other than that, another new mysterious magnetic transition was observed in the temperature-dependent magnetization and AC susceptibility curves below the PM transition temperature. Initially, we predicted the development of a Skyrmion-like phase by observing such anomalies in the magnetization curves. For confirmation, we studied isothermal $\chi'_{ac}(H)$ and $\chi''_{ac}(H)$, where several distinct phase boundaries were observed with the application of small perturbation distinguishing whirl-like magnetic Skyrmion phase surrounded by different magnetic regions. Further, we summarized all the magnetic phases as *H-T* phase diagrams introduced by the spin frustration and the field dependency on the complex spin structure. The Skyrmion phase (S) was evidently demonstrated in the *H-T* phase diagrams enclosed by H_{A1}, H_{A2}, T_{A1} and T_{A2} in Figure 6.9 (a, b, c) for the present system. Interestingly, with a larger doping concentration of Se atoms the Skyrmionic phase space is expanding vibrantly. The enhancement in the temperature range of the complex magnetic structure is introduced by reorientation of the spins due to the tension created on the crystal chemically by the replacement of Se over S. Significant enhancement of the temperature stability of the Skyrmions may also results in a noticeable expansion of the helical propagation vector. However, the consequence in the proportion of Se substitution causes a modest augmentation in the thermal stability of the Skyrmions can be enlightened by the Dzyaloshinskii-Moriya interaction strength modulated by the competition among different magnetic alignments. This phenomenon unswervingly affects the stabilization of the Skyrmionic phase in the Kagome ferromagnet positively even at such a small size, presenting such materials to become the information carriers in the forthcoming spintronics devices. Our accomplishment associated with the extension of the mysterious magnetic

phase with the application of an exceptionally small magnetic field under chemical pressure initiated by interstitial dislocation conveys $Co_3Sn_2S_{2(1-x)}Se_{2x}$ as a potential candidate to be applied in spintronics devices.